Journal of Magnetism and Magnetic Materials 462 (2018) 13–21

Contents lists available at ScienceDirect

Journal of Magnetism and Magnetic Materials

journal homepage: www.elsevier.com/locate/jmmm

Yerba Mate applications: Magnetic response of powders and colloids of iron oxide nanoparticles coated with *Ilex paraguariensis* derivatives

D. Fabio Mercado [a], Mariano Cipollone [b], Mónica C. González [a], Francisco H. Sánchez [c,*]

[a] Instituto de Investigaciones Físicoquímicas Teóricas y Aplicadas, Universidad Nacional de La Plata-CCT La Plata, CONICET, Argentina
[b] Y-TEC YPF Tecnología, S.A. Baradero S/N, 1925 Ensenada, Bs As., Argentina
[c] Instituto de Física de La Plata, Universidad Nacional de La Plata-CCT La Plata, CONICET, Argentina

ARTICLE INFO

Article history:
Received 21 December 2017
Received in revised form 7 April 2018
Accepted 21 April 2018
Available online 25 April 2018

Keywords:
Nanoparticles
Core-shell
Iron oxide
Ilex paraguariensis
Dipolar interactions
Coercive field

ABSTRACT

A co-precipitation synthesis method was used to obtain iron oxide nanoparticles coated with Yerba Mate (*Ilex paraguariensis*) extract. These particles have a core–shell structure with the iron oxide phase surrounded by an organic shell provided by an organic component which come from the Yerba Mate extract.

Obtained nanoparticles were exhaustively characterized as powders and in aqueous colloidal suspensions using several techniques such as TEM, XRD, SAXS, TGA, ATR-FTIR, Raman and XPS spectroscopy, magnetic moment measurement and specimen ac susceptibility. All results together show that the obtained particles are single-crystal iron oxide particles with magnetite as the most probable phase. Yerba Mate extract shell mass to iron oxide core mass, m_S/m_c, could be increased up to 6.2×10^{-2}, depending on the synthesis conditions. As a function of m_S/m_c the crystallite size of the nanoparticles decreased from about 15 nm to 11 nm, while saturation magnetization Ms and coercive field Hc of powders decreased. Ms. diminution was associated to increasing modification of core surface electronic states due to chemical bond of iron in iron oxide to Yerba Mate extract components; on the other hand, coercivity reduction was modelled on the basis of the increasing interparticle separation and dipolar interaction weakening, which occurs as shell thickness grows.

Differences between the particle core mean size obtained with TEM, SAXS, XRD and magnetic measurements are observed. The fact that magnetic size was smaller than particle and crystallite sizes was attributed to the existence of intense dipolar interactions. It was found that low field susceptibility in a colloid sample was about 2.5 times that of the powder specimen, a result that shows that demagnetizing effects prevail in the powder specimen, while they may be absent in the colloid due to the larger interparticle mean separation expected in the latter. Analysis of powder and colloid susceptibility was done based on a recently developed model was in agreement with the one performed for the coercive field behaviour.

1. Introduction

Iron oxide nanoparticles are currently one of the most promising materials because of their multiple technological applications in electronic devices, the environment, and biomedicine [1–7]. In order to enhance the performance of iron oxide nanoparticles, they must satisfy minimal cytotoxicity, excellent colloidal stability, suitable particle shape and size distribution [8]. The performance of these materials is dependent not only on the size and morphological characteristics of the particles but also on the nature of the coating materials [9]. In fact, control of the surface chemistry of magnetic nanoparticles should meet specific demands to achieve the necessary domains of applications.

The uses of iron oxide nanoparticles coated with organic shells as adsorbents and catalysts has been intensively studied during the last decades in an increasing number of environmental applications [10]. In general, organic coating of iron oxide nanoparticles promoted an enhanced adsorption capacity and improved catalysis performance. Moreover, the use of organic molecules as templates during the synthesis of iron oxide, leads to less crystalline nanostructures and improves the particles stability and compatibility in aqueous suspensions. Surface stabilization with humic substances, biomolecules, photosensitizers, and plant extracts, among others, have been reported [3,11–14]. The *Ilex paraguariensis*, familiarly known as Yerba Mate, is an Argentinean plant heavily marketed in South America because it is typically used to prepare

* Corresponding author at: Departamento de Física-UNLP, Casilla de Correos 67, 1900 La Plata, Argentina.
E-mail address: sanchez@fisica.unlp.edu.ar (F.H. Sánchez).

https://doi.org/10.1016/j.jmmm.2018.04.048
0304-8853/

infusions with wide acceptance in the regional population. Despite its spanned use, there is only one report on the synthesis of iron oxide nanoparticles coated with an organic shell which comes from the Yerba Mate hydrosoluble extracts and it is a parallel study of this paper [15]. However, a magnetic characterization of the obtained particles has not been done yet and this is the main scope of this paper.

In particular, control of saturation magnetization and susceptibility are of crucial importance for the particles technological applications. Single domain iron oxide nanoparticles in the form of magnetite or maghemite, bear a large magnetic moment of the order of 10^3 to 10^5 Bohr magnetons. They present magnetic anisotropy and moment relaxation mechanisms specific to the nanoscale but may be strongly affected by shape, surface chemistry and interactions between particles. Dipolar magnetic interactions between particle moments have a strong influence on moment relaxation [16,17] and susceptibility [18–20]. Interactions promote particles aggregation. In colloids of particles with sufficiently high moment low energy configurations such as chains and loops tend to form. It has been shown that shape and size of low energy configurations are strongly dependent on the intensity of an applied magnetic field [21]. Non-magnetic coating produces a steric repulsive barrier between particles, therefore reducing the intensity of interactions.

Despite the numerous investigations on the effect of organic coating on the particles properties, a comparative study on the impact of organic shells on iron oxide magnetic properties has yet not been performed. In this context, herein we report the synthesis of iron oxide nanoparticles, most probably in the form of magnetite (*vide infra*) coated with different amounts of the hydrosoluble extract of Yerba Mate and analyze the modification of the materials magnetic properties as a function of the mass ratio between the organic shell and the iron oxide core, m_s/m_c.

2. Experimental

2.1. Synthesis

The Yerba Mate (YM, *Ilex paraguariensis*) extract used on this synthesis was prepared mixing 10 g of YM with 1 L of water at 70 °C. The temperature was maintained at 70 °C during one hour and the suspension was stirred vigorously. Then, the supernatant was separated through a filtration process ($\varnothing$ = 0.22 μm) to eliminate any solid present in the extract. The solution was kept in 4 °C Before being used.

The coated iron oxide nanoparticles with YM extract were prepared optimizing reported methods for magnetite synthesis [15]. 6,1 g $FeCl_3{\cdot}6H_2O$ and 4,2 g $FeSO_4{\cdot}7H_2O$ were dissolved in 100 mL of deionized water. The resulting solution was heated to 90 °C and followed with the addition of 10 mL of NH_4OH 25%, immediately after 50 mL of diluted solution with different amounts of extract were added (0–20–60–100% v/v). The resulting suspension was kept at 90 °C for 30 min under stirring and then was cooled to 25 °C. The magnetic powder was separated from the liquid using a laboratory magnet and the solid was washed several times with deionized water until no remaining organic extract was detected in the washing liquors by UV/spectroscopy and total organic carbon analyser. Finally, the black powders were dried in vacuum oven at 70 °C during 24 h and then stored at room temperature. Depending on the amount of extract used in the synthesis, materials were named YMA (0% v/v), YMB (20% v/v), YMC (60% v/v) and YMD (100% v/v). All commercial products used were purchased from Sigma-Aldrich and used with no further purification process. The Yerba Mated used was brand "*El playadito*" production batch N° 45-03. Colloidal suspensions were prepared with distilled water at pH 6.5–7.0 under ultrasound application. Nanoparticle (NP) concentrations were of 75 ppm or less. Suspensions remained stable for days while kept at 4–8 °C in a refrigerator.

2.2. Characterization

High Resolution Transmission Electron Microscopy (HRTEM) images were obtained using a JEOL 1200EX II microscope with maximum magnification x200000.

X-ray analyses were carried on a θ-2θ Philips 3020 powder diffractometer with a PW 3710 controller, using Cu-Kα radiation, sweeping θ from 20° to 80° at 0.01°/s.

SAXS studies were performed using a XEUSS 1.0 HR (XENOCS, Grenoble) device equipped with a microfocus X-ray source and a Pilatus 100 K detector (Dectris, Switzerland). The scattering intensity (in arbitrary units) was recorded as a function of the scattering vector $q = (4\pi/\lambda)\sin\theta$, where λ is the radiation wavelength (1.5419 Å) and 2θ the scattering angle. Scattering profiles were analysed using SASfit software package.

Thermogravimetric Analysis (TGA) was performed using a Q600 TA Instruments device. Analysis was performed under an air environment (100 cm^3/s), after one minute at initial temperature of 323 K, following a 10 K/min ramp up to 1273 K, and maintaining this temperature for 10 min.

Magnetic moment was measured versus applied field using a LakeShore 7304 vibrating sample magnetometer (VSM), varying the field within the interval $[-1{,}51 \times 10^5,\ 1{,}51 \times 10^5]$ A/m. VSM experimental time window was $\tau_{VSM} \approx 30s$.

Specimen ac susceptibility was determined by measuring magnetic moment as a function of temperature (30 K < T < 325 K) under an applied field of amplitude of 80 A/m and a frequency $f = 825Hz$. In this case experimental window was $\tau_{ac} = 1/\omega$, with $\omega = 2\pi f$.

Specimens for magnetic studies were prepared as follows. Powders: about 60 mg of NPs were wrapped with a clear pvc thin film and firmly placed into a 5 mm long gelatine capsule. Colloids: 50 μL of a 75 ppm Np suspension were placed into a 4 mm wide clear heat-shrinkable tube and sealed into a 5 mm long bag. Bags of fluid were kept refrigerated at $T \approx 277K$ until few minutes before the initiation of measurements to avoid colloid destabilization. Capsule (or bag) was firmly inserted into a clear drinking straw which was fixed to the end of VSM driver or ac susceptometer probe. In the case of VSM experiments, specimen bag was kept oscillating at the magnetometer frequency of 82 Hz for 30 min before starting moment measurement in order to promote uniformity of the NPs distribution within bag volume. For the same reason, in the case of ac susceptometry experiments, specimen bag was submitted to ultrasound vibration for ten minutes at room temperature before attaching it to the measurement probe, then it was immediately inserted into the device and cooled down below water freezing temperature.

3. Results

3.1. TEM, SAXS, XRD and TGA

Fig. 1 shows typical HRTEM images of YMA and YMD nanoparticles. For both samples the nanoparticles have a quasi-spherical geometry.

From a set of similar images of each sample, a corresponding histogram of NP diameters was built from the size measurement of 400 well-dispersed NPs (see figure inset for each case), from which mean core diameters of (14.9 ± 1.3) and (13.9 ± 1.6) nm were obtained from the fitting to a normal distribution (solid lines) for YMA and YMD samples. Thus indicating that under the conditions studied here, the use of different amount of Yerba Mate

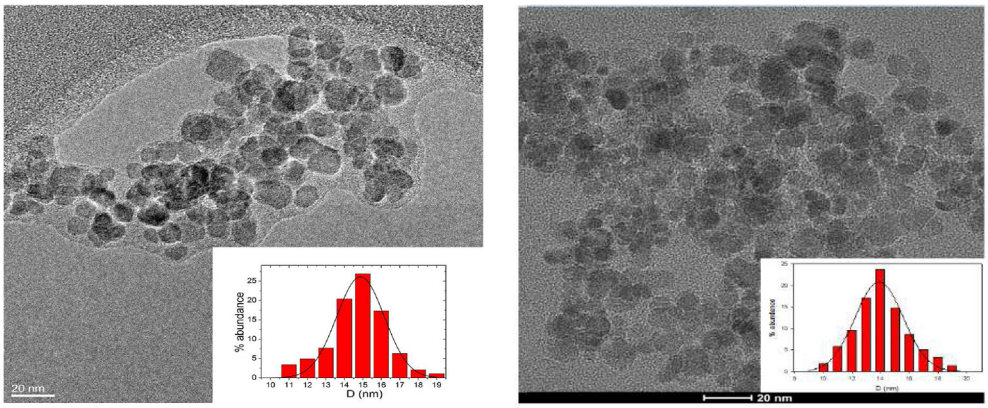

Fig. 1. HRTEM image for YMA (left) and YMD (right) sample with their corresponding individual particle size distribution.

extract does not affect significantly the individual particle size distribution of the iron oxide nanoparticles. Fig. S1 shows another HRTEM image of YMD sample where it is possible to appreciate crystalline planes with a space of ~2.6 Å which are in line with the plane d_{311} plane of magnetite or maghemite (*vide infra*).

Table 1 shows the result of the fit realized on SAXS data with the unified Becauge model [22,23] in which the scattered X-ray intensity it is related with the rotation radius Rr. This parameter corresponds to the particle volume plus the solvent volume which rotates jointly with it. The analysis of these results indicate the existence of aggregates with around a mean rotation radius of $Rr_2 \approx 26$ nm with a surface with fractals characteristics ($N < 4$). The presence of globular particles with a $Rr_2 \approx 5.5$ nm with a well-defined soft surface ($N < 4$). These results are in agreement with the geometry observed in the TEM results (*vide supra*). The geometric particle diameter of each sample (shown in Table 1) have been calculated following the same model where $D = 2\ Rr$ assuming that the particles are spherical. These values are in agreement with the ones obtained in the TEM experiments. In general, the SAXS results indicates that under the conditions here studied, there is no significant changes in the particles size or shape for all samples none in the aggregates that they form.

TGA results [15] allowed determination of the ratio mass shell (coating) to mass core (iron oxide), ms/mc, which ranged from 0.002 to 0.062 (values are also listed in Table 2) from which the thickness of the shell was estimated for each specimen as it will be discussed below.

The XRD technique was used in order to determine the presence of iron-oxide crystalline network in all samples [15]. Fig. 2 shows the diffractogram of only the YMC specimen, but all samples present the same pattern.

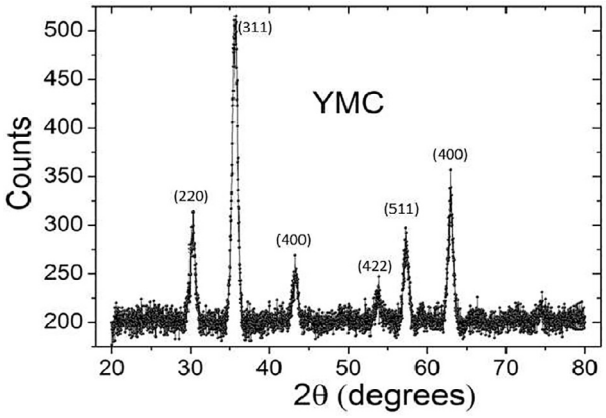

Fig. 2. X-ray diffraction from YMC specimen.

Table 1
Parameters of the Unified Becauge model applied over the scattering curves in SAXS experiments. The * indicate that the values were kept constants during the fitting.

Parameter	YMA	YMB	YMC	YMD
Rr_1 (nm)	5.67 ± 0.03	5.60 ± 0.04	5.28 ± 0.04	5.47 ± 0.08
N_1	3.33 ± 0.03	3.94 ± 0.02	4*	4*
Rr_2 (nm)	27.6 ± 0.30	25.8 ± 0.30	24.9 ± 0.30	26.0 ± 0.50
N_2	3.07 ± 0.04	2.86 ± 0.05	2.84 ± 0.04	2.80 ± 0.07
Individual particle diameter (nm)	14.64 ± 0.06	14.46 ± 0.08	13.63 ± 0.08	14.12 ± 0.16

Table 2
Relevant quantities obtained from physical characterization of YM coated iron oxide NPs, m_s/m_c: shell mass to core mass ratio, H_C: coercive field, $\langle D_X \rangle$: crystallite mean diameter, $\langle \mu \rangle$: mean apparent magnetic moment, σ_μ: LogNormal associated sigma parameter in powders, N: NPs per volume unit, $\langle D_p \rangle$: magnetic apparent diameter in powders, $\sigma_{\langle D \rangle}$: LogNormal associated sigma parameter, M_S: NP saturation magnetization, κ_p: apparent susceptibility of powders, $\langle D_c \rangle$: mean apparent diameter in colloid D, $\langle D_S \rangle$: NP core diameter determined by SAXS and ε_{Ds}: its typical uncertainty, $\langle D_{TEM} \rangle$: mean apparent diameter obtained by TEM and ε_{TEM}: its typical uncertainty.

spec	ms/mc	H_C (A/m)	$\langle D_X \rangle$ (nm)	$\langle \mu \rangle$ (μ_B)	σ_μ	N ($1/m^3$)	$\langle D_p \rangle$ (nm)	$\sigma_{\langle D \rangle}$	M_S (A/m)	κ_p	$\langle D_c \rangle$ (nm)	$\langle D_S \rangle$ (nm)	ε_{Ds} (nm)	$\langle D_{TEM} \rangle$ (nm)	ε_{TEM} (nm)
YMA	0.000	833	14,8	1.62e4	0.55	2.05e24	9.8	0.18	3.07e5	6,3		14,6	0.1	14,9	1,3
YMB	0.009	699	12,1	1.73e4	0.54	1.87e24	10.1	0.18	2.98e5	6,5		14,5	0.1		
YMC	0.033	411	11,6	1.71e4	0.55	1.80e24	10.2	0.18	2.85e5	6,1		13,6	0.1		
YMD	0.062	110	11,3	1.28e4	0.85	2.42e24	9.2	0.28	2.88e5	7,1	12,5	14,1	0.2	13,9	1,6

It can be evidenced the presence of six peaks: 30.2° (2 2 0), 35.6° (3 1 1), 43.0° (4 0 0), 53.9° (4 2 2), 57.3° (5 1 1) and 62.9° (4 0 0) that could be attributed to the magnetite or maghemite phases (see for example, standard X-ray data card number 11-0614, ICCD database). However, these peaks could indicate the presence of a maghemite phase, due that both iron oxides have the same cubic structure and their lattice parameters are almost identical [24]. The pattern confirms the spinel structure of crystals, and is consistent with the presence of magnetite or maghemite phases. XPS and Raman studies on these specimens (not shown) indicate that the Fe oxide is most probably magnetite [15].

The average crystallite sizes were estimated using the Scherer's equation with $\lambda = 0.154$ nm, assuming that the nanoparticles are completely spherical, a shape factor $k = 0.94$, and the FWHM of the peaks at $2\theta = 35.5°$. Their values ranged from 14.8 to 11.3 nm and are also listed in Table 2. The generally smaller crystalline domain size obtained from XRD in comparison to the core diameter obtained from SAXS and TEM suggests that the Fe oxide core has a crystalline nucleus surrounded by a disordered or amorphous near surface region and that each particle is a single crystal. Therefore, the obtained NPs may be thought as an iron oxide crystal, surrounded by a disordered Fe oxide layer which in turn is coated with the YM derivatives.

3.2. Magnetic characterization

3.2.1. Powder specimens

Fig. 3 shows room temperature magnetization versus applied field curves of the powders of the obtained NPs. The specimen specific magnetization in Am^2/kg was obtained as the ratio of measured specimen moment and mass. The iron oxide cores specific magnetization was derived by correcting previous quantity for the relative mass m_s/m_c of YM shell to iron oxide core (see Table 2). Volumetric core magnetization M versus the applied field H was obtained by dividing specific magnetization by the spinel iron oxide density (taken as 5.2×10^3 kg/m^3). Insets of Fig. 3 show that all specimens present coercivities of less than 820 A/m, which decrease as m_s/m_c increases, from YMA to YMD specimens (see Fig. 3, left inset).

Anhysteretic M vs. H curves for powder specimens, built following the procedure reported in the literature [25], are shown in Fig. 4. In the reference, authors demonstrated that for dense NP arrangements, coercivity originated in dipolar interactions between NPs can be eliminated with this procedure. They showed that curves constructed by averaging the two branches of M, i.e.,$M(H) = (M_{up}(H) + M_{low}(H))/2$ where M_{up} and M_{low} are the upper and lower branches of the hysteretic magnetization, coincide with a purposely measured anhysteretic curve. Top inset in Fig. 4 illustrates a typical analysis of an anhysteretic M vs. H curve (in the example for YMA) using the fitting function

$$M(H,T) = N \int \mu \left(\coth\left(\frac{\mu_0 \mu H}{kT}\right) - \frac{kT}{\mu_0 \mu H} \right) f(\mu) d\mu + \chi_l(T) H \qquad (1)$$

where $\chi_{l\ is}$ the high field linear susceptibility. This term combines negative contributions due to the diamagnetic responses of the NP shell and of specimen wrapping and encapsulation (and water in the case of colloids) with a positive contribution due to the potential existence of a magnetically frustrated layer located in the surface of the NPs core or paramagnetic ions in the colloids. $f(\mu)d\mu$ is the normalized number of NP moments in the interval $\mu, \mu + d\mu$. For the analysis, a Lognormal distribution was used. Bottom inset in Fig. 4 shows apparent susceptibilities κ obtained from the analysis of the central linear region of these curves. Table 2 displays values of saturation magnetization M_S, mean number of NPs per unit volume N, mean NP moments $<\mu>$, mean magnetic NP diameters $<D_p>$ (assuming $V_P = \mu/M_S$) and the standard deviations σ_μ and σ_D of $\ln(\mu)$ and $\ln(D_p)$, respectively, retrieved form fits. Fig. 5 shows the NP diameter Lognormal distributions.

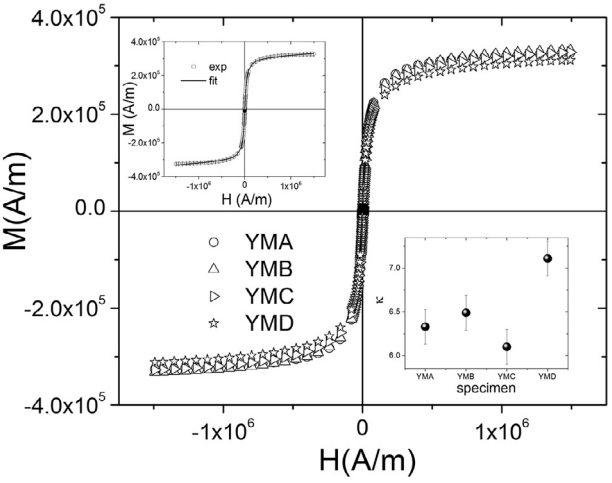

Fig. 4. Anhysteretic M vs H cycles for the four powder specimens at room temperature. Top-left: fitted cycle. Bottom-right: low field susceptibilities.

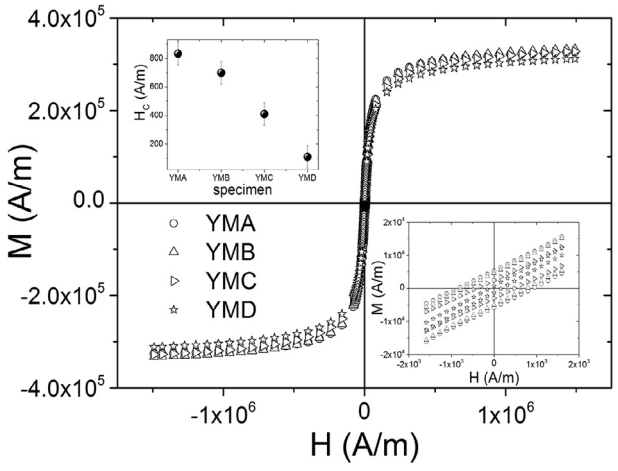

Fig. 3. M vs H cycles obtained from the four powder specimens at room temperature. Top-left: coercive field values. Bottom-right: detail of the cycles central region.

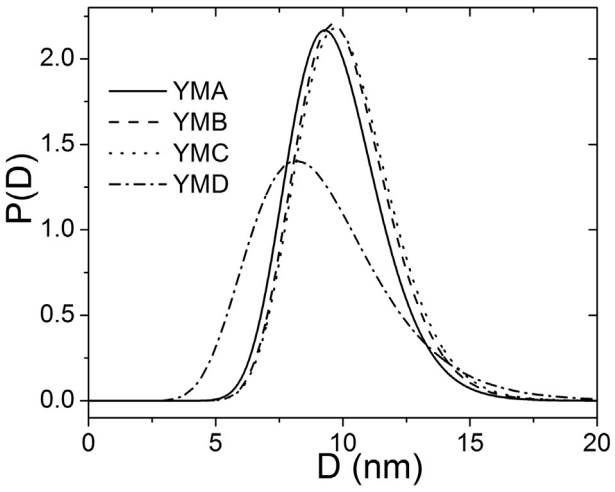

Fig. 5. Magnetic apparent diameter distributions obtained from fitting of cycles of Fig. 4 with Eq. (1).

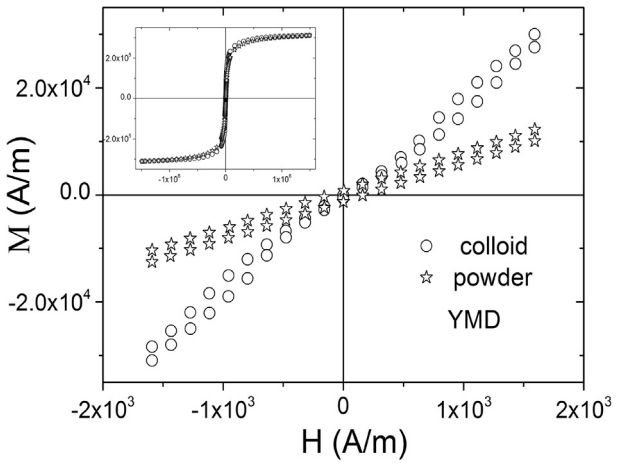

Fig. 6. Comparison of the magnetic response of YMD specimen in powder (stars) and stable colloid (circles) forms. Main graph is an enlargement of the central part of the complete M vs H cycle shown in the inset.

It is remarkable that mean SAXS diameters are about 40% larger than mean magnetic ones, i.e. $\langle D_S \rangle \approx 1.4 \langle D_P \rangle$ while crystallite sizes to magnetic ones ratio vary form 1.13 (YMC) to 1.51 (YMA).

3.2.2. YMD colloid specimen

Fig. 6 presents *M* vs. *H* curves obtained from YMD specimens in powder and colloid forms. A remarkable difference is observed between experimental (apparent) initial susceptibilities in both specimens, whose origin will be discussed later; they are $\kappa_p = 7.1$ and $\kappa_c = 17.7$, respectively. The much higher susceptibility of the colloid is confirmed by ac susceptibility measurements performed on the same specimens (see Fig. 7). Both in phase and out of phase components of κ reflect this behaviour in the whole temperature range of measurement. A sudden change in the magnetic response of the colloid is clearly observed at water temperature melting point.

In phase apparent susceptibility κ' takes values of $\kappa\prime_p \approx 5.7$ and $\kappa\prime_c \approx 11.5$ at 273 K, for powder and colloid respectively. It should be pointed out that value of $\kappa\prime_c$ corresponds to the frozen colloid and should not be directly compared to that recorded in the molten specimen. At 300 K powder susceptibility ($\kappa\prime_p \approx 6$) is in acceptable agreement with the value obtained from M vs. H curve at the same temperature ($\kappa_p \approx 7.1$), but molten colloid susceptibility ($\kappa\prime_c \approx 7.4$) is far below from the value retrieved from *M* vs. *H* ($\kappa_c \approx 17.7$).

Recorded out of phase susceptibility κ'' presents maxima between 180 and 200 K which can be ascribed to the process of NP magnetic moment unblocking. It is remarkable that ratio of dissipative components reaches a large ratio $\kappa''_c/\kappa''_p \approx 3.3$ at $T \approx 194K$. Temperature of κ'' maximum can be taken as a quasi-direct measurement of mean blocking temperature T_B [26]. One remarkable feature of these results is that blocking temperatures of colloid and powder clearly differ by about 13 K, even being both in the solid state ($T_B^c \approx 195K > T_B^p \approx 182K$).

4. Discussion

There are evidences in the literature that dipolar interactions modify the relaxation time and coercivity of single domain magnetic NPs [16,27,28]. In most cases it has been reported that interactions increase the energy barrier for magnetic moment fluctuation and consequently increase coercivity [29,30]. In the present study coercivity decreases with shell to core mass ratio m_s/m_c, i.e. from YMA to YMD specimens (Fig. 3, insets). Increasing m_s/m_c implies increasing shell thickness d_{YM}, and therefore larger intercore distances in powder specimens. For NPs in contact, near neighbour distance will be of the order of $2(d_{YM} + R_S)$, where R_S is the SAXS radius $R_S = D_S/2$. Assuming that H_C has dipolar origin [31] it must depend on d_{YM} as $(d_{YM} + R_S)^{-3}$, which for small $x = d_{YM}/R_S$ can be approximated by

$$H_C \propto (d_{YM} + R_S)^{-3} \propto (1 + x)^{-3} \approx b(1 - 3x)/R_S^3,$$

On the other hand a relationship between m_s/m_c and x can be stablished as

$$\frac{m_s}{m_c} = \frac{\rho_s V_s}{\rho_c V_c} = \frac{\rho_s}{\rho_c}[(1 + d_{YM}/R_S)^3 - 1] \approx -3\frac{\rho_s}{\rho_c}x$$

where V_s and V_c are the volumes of shell and core, and ρ_s and ρ_c their densities, respectively. x is retrieved form last equation and replaced in the former one to get

$$H_C \approx \frac{b}{R_S^3}\left(1 - \frac{\rho_c}{\rho_s}\frac{m_s}{m_c}\right).$$

Last expression can be used to estimate ρ_s, by analyzing H_C values using b and ρ_s as fitting parameters (see Fig. 8). Value retrieved for the shell density is $\rho_s \approx 370 kg/m^3$. This density should not be interpreted as the YM derivatives one, but rather as an effective value corresponding to the average between carbonaceous chains and vacuum in the space among them. If $\rho_{YM} \approx 1 \times 10^3 kg/m^3$, then about 60% of the shell volume would be empty space.

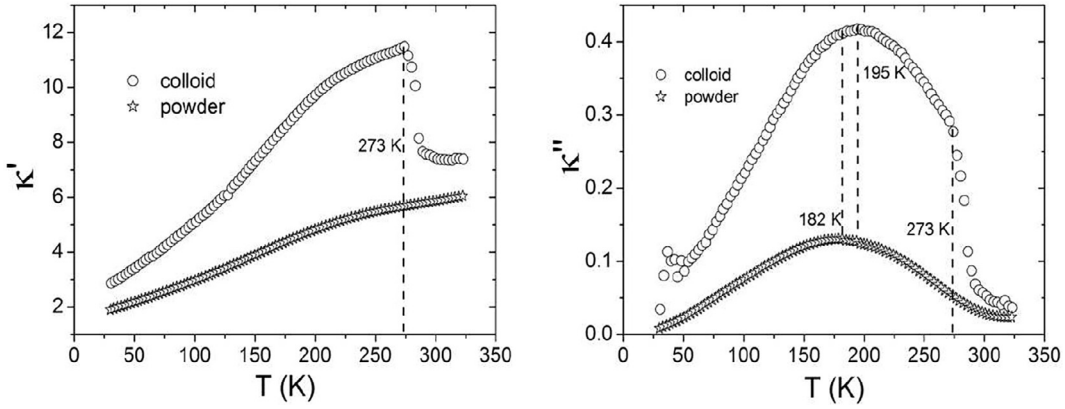

Fig. 7. In phase (a) and out of phase (b) components of the ac susceptibility for YMD powder and colloid specimens.

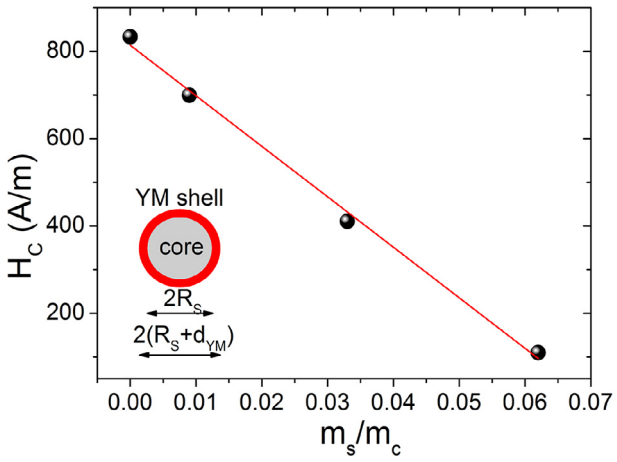

Fig. 8. Analysis of coercive field values with core/shell model.

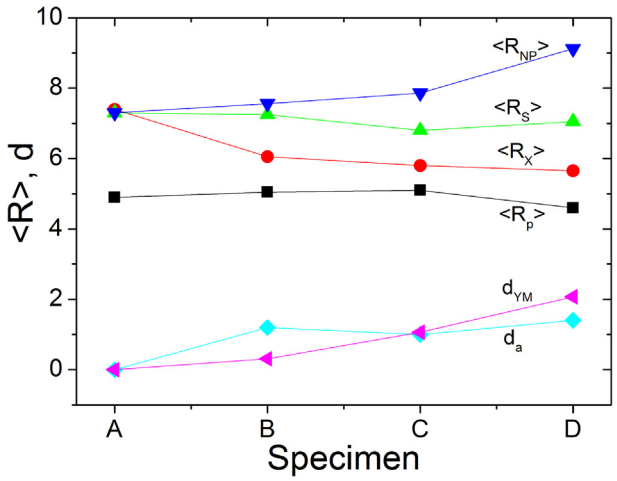

Fig. 9. Characteristic mean radii of YM coated iron oxide NPs: total radius (<R_{NP}> = <R_S> + d_{YM}), iron oxide core radius (<R_S>, SAXS), crystallite radius (<R_X>, XRD), apparent magnetic radius (<R_p> from M vs. H), YM layer thickness d_{YM}, core surface disordered layer d_a.

Once ρ_s has been estimated x is obtained from

$$x \approx -\frac{1}{3}\frac{\rho_c}{\rho_s}\frac{m_s}{m_c}$$

And d_{YM} is in turn calculated. Fig. 9 displays all characteristic sizes associated to YM coated NPs: apparent (magnetic, powders), crystal, core, and whole NP sizes, as well as estimates of d_{YM} and disordered region d_a thicknesses. Assuming NPs in contact with each other, this result corresponds to a mean intercore distance relative to NP diameter, $\gamma_S = D_{NP}/D_S$, which varies in the interval $1 \leqslant \gamma_S \leqslant 1.29$, or a mean relative intercrystal distance $\gamma_X = D_{NP}/D_X$ varying within the range $1 \leqslant \gamma_X \leqslant 1.61$ (specimens YMA to YMD).

The existence of non-negligible dipolar interactions indicates that measured susceptibility must be considered "apparent" in the sense that it is not intrinsic of individual NPs. In the case of random dispersions of NPs in solids and powders of NPs, dipolar interactions have a demagnetizing character and reduce susceptibilty [18,19]. In the present case, the decreasing intensity of these interactions with m_s/m_c ratio is consistent (within experimental error) with the behaviour of apparent initial susceptibility κ presented in Table 2 and in inset of Fig. 4. In this sense, comparison of apparent initial ac susceptibilities obtained from powder and colloid forms of YMD specimen, shown in Figs. 6 and 7, is enlightening.

The fact that $\kappa_c > \kappa_p$ suggests that dipolar interactions are absent in the colloid or at least greatly reduced. However, the scenario could have been different. It has been demonstrated that interactions induce low energy structures in NP colloids, especially linear arrangements like NP chains [21]. In these arrangements dipolar field is magnetizing, i.e. increases effective field on NPs leading to apparent susceptibilities higher than intrinsic or true ones. One criterion which can be used to decide whether magnetizing or demagnetizing effects are present is to compare NP magnetic (apparent) size with NP core size retrieved from high resolution TEM, SAXS and iron oxide crystallite size determined by XRD experiments. Non interacting NPs respond with their intrinsic (true) susceptibility

$$\chi = \frac{\mu_0 \langle V \rangle M_S^2}{3kT} \tag{2}$$

while their apparent susceptibility, i.e. When interactions cannot be neglected, can be approximated by

$$\kappa = \frac{\mu_0 \langle V_{app} \rangle M_S^2}{3kT} \tag{3}$$

where $\langle V_{app} \rangle$ is the apparent NP mean volume. In the case of YD sample, from ($\kappa_c \approx 17.7$) a mean apparent magnetic size (D_c) ≈ 12.5 nm is obtained for the colloid which has to be compared with $\langle D_p \rangle \approx 9.2$ nm retrieved from the powder and with $\langle D_S \rangle \approx 14.1$ nm and $\langle D_{TEM} \rangle \approx 13.9$ nm.

The ac susceptibilities recorded from the YMD colloid show two differences with those obtained from dc M vs. H measurements. While $\kappa_c/\kappa_p \approx 2.5$ was measured by dc magnetometry at 300 K, ac susceptometry results were in the ratios $\kappa\prime_c/\kappa\prime_p \approx 2.0$ (273 K, frozen colloid) and $\kappa\prime_c/\kappa\prime_p \approx 1.2$ (300 K, molten colloid). The sensible reduction of colloid to powder susceptibility ratio from 2.5 to 2.0 may obey to at least two causes. Firstly, in the frozen colloid Brown relaxation (the mechanism of NP magnetic moment fluctuation by NP rotation) is absent. Therefore, if Brown relaxation plays a role in the dynamics of colloid magnetization above 273 K, NP magnetic response should be affected if this mechanism is supressed. Secondly, protocols of ac and dc measurements present major differences: ac measurement was performed under a small oscillating field with an amplitude of 80 A/m which was applied after the specimen became frozen. A few minutes passed between the last time when colloid was homogenized and the moment in which was frozen. On the other hand, dc susceptibility has been measured while colloid was continuously agitated at 82 Hz, in the linear M vs. H region, after submitting the specimen to a field of more than 1.5×10^5 A/m. Besides the homogenizing effect of the magnetometer probe vibration, it has been reported that high enough fields may induce the formation of low dipolar energy structures, like long NP chains with thicknesses of several NP diameters [32,33]. Therefore, demagnetizing effects could be less important, or even compensated by magnetizing ones, in the case of dc measurement, giving rise to a considerably larger apparent susceptibility.

The drastic decrease of colloid susceptibility above melting temperature is a consequence of a well-known problem of colloid stability. Magnetic aqueous colloids bear a strong tendency to unstabilize after being frozen. When temperature increases above 273 K YMD colloid unstabilize and NPs accumulate at the bottom of the plastic bag. This fact decreases interparticle distances and increases dipolar interactions to an extent close to that occurring in the powder specimen. The presence of surrounding liquid and the fact that sample switches position between the two susceptometer sensor coils approximately every 30 s has prevented complete aggregation of the NPs and therefore susceptibility was slightly larger than in the powder specimen, i.e. $\kappa\prime_c/\kappa\prime_p \approx 1.2$.

After the following simple analysis, we may conclude that measured colloid susceptibility is closest to NP intrinsic one, since it leads to magnetic sizes which are closer to crystal ones determined by means of structural techniques. On one hand, extrapolating ac results to 300 K we obtain $\kappa_c \approx 11.7$ which corresponds to $\langle D_c \rangle \approx 10.9nm$, i.e. slightly larger than values reported in Table 2 for powder specimens. On the other hand, using $\kappa_c \approx 17.7, \langle D_c \rangle \approx 12.5nm$ is obtained, value which is in better agreement with SAXS (14.1 nm) and XRD (11.3 nm) results. To put these results in a better perspective we must consider that XRD provides an estimation of the iron oxide crystallite size while SAXS gives and estimation of the whole magnetite core. If, as happens usually, iron oxide core has a crystalline nucleus and a disordered near surface region, XRD sizes would be smaller than SAXS ones, as occurs in our case. Additionally, it has been reported that the disordered surface region presents a lower magnetic specific response, in comparison to the crystalline nucleus [34]. Therefore it is reasonable that $\langle D_P \rangle \leqslant \langle D_X \rangle \leqslant \langle D_S \rangle$ (see Fig. 9).

In conclusion, interaction between NP dipolar moments in powder specimens gives rise to a decrease of measured (apparent) susceptibility. As a consequence, NP apparent sizes $\langle D_P \rangle$, derived from susceptibilities are smaller than actual ones. Since NPs are densely packed in powders, this effect is notorious in specimens prepared in this form and with no YM coating (YMA). When specimens are well dispersed in a colloid (YMD) apparent magnetic size $\langle D_c \rangle$ lays above XRD one, but below SAXS one, suggesting that magnetizing dipolar effects slightly prevail.

Demagnetizing effects can be described by an effective demagnetizing tensor which depends on specimen shape, interparticle relative distance γ, and on other details of NPs distribution within the specimen [10,16]. For a uniform spatial distribution of NPs, as the one approximately existing in a dense powder specimen, the effective demagnetizing factor along a specimen principal direction $\hat{u}$ can be written as

$$N_{eff,u} \approx \frac{\varphi}{\gamma^3} N_{s,u} \tag{4}$$

where φ is the NPs packing fraction (assumed here to be $\varphi \approx 0.7$), and $N_{s,u}$ is the demagnetizing factor associated with specimen shape [35]. In our case specimen had the shape of a nearly square prism (~2 mm × 2 mm × 4 mm) and it was measured along the shortest axis for which [36] $N_s \approx 0.4$. $N_{eff,u}$ is related to specimen susceptibilities by [37]

$$N_{eff} = 1/\kappa - 1/\chi,$$

expression which, using Eqs. (2) and (3) can be rewitten as

$$N_{eff}^S \approx (1 - (\langle D_P \rangle / \langle D_S \rangle)^3)/\kappa$$

$$N_{eff}^X \approx (1 - (\langle D_P \rangle / \langle D_X \rangle)^3)/\kappa.$$

Solving Eq. (4) for γ its value can be estimated. Results for N_{eff}^S, N_{eff}^X, γ_S band γ_X are displayed in Table 3 for the four specimens.

Table 3
Effective demagnetizing factors in the measurement direction and mean relative interparticle distances for powder specimens, considering that magnetic response comes from NP core (S, SAXS diameter) or from NP crystal nucleus (X, XRD).

	N_{eff}^S	N_{eff}^X	γ_S	γ_X
A	0,11	0,11	1,36	1,36
B	0,1	0,06	1,4	1,63
C	0,1	0,05	1,44	1,75
D	0,1	0,06	1,4	1,63

Both γ_S and γ_X compare well with the ones estimated previously for YMD, when coercivity behaviour was analysed, $\gamma_S \approx 1.29$ and $\gamma_X \approx 1.61$. From the previous discussions we may conclude that NP magnetic core is essentially its crystallite part. The fact that apparent sizes are smaller than crystallite ones except in the case of YMD colloid specimen (dc measurement), indicates that demagnetizing effects prevail in the powder but they may be absent in the liquid. In fact, a mild magnetizing effect may dominate in the latter.

A rapid estimation based on colloid concentration shows that theoretical average interparticle distance would be of the order of several NP diameters if NPs were homogeneously dispersed in the colloid, hence these results suggest that aggregates may exist [38]. This conclusion is in agreement with the SAXS results presented here which demonstrate the presence of fractal-like arrangements with sizes of about 30 nm. To explain the mild magnetizing effect, these arrangements would be sets of chain-like objects, which can orient parallel to the applied field, as has been experimentally observed [21,39].

Mean blocking temperatures $T_B^p \approx 182K$ and $T_B^c \approx 195K$, determined for YMD powder and colloid specimens, respectively, indicate that NP Néel relaxation time, given by

$$\tau = \tau_0 \exp(K_{eff} V/kT),$$

approaches the inverse of susceptometer angular frequency $\omega^{-1} = (2\pi f)^{-1} = 1.93 \times 10^{-4} s$ at each of those two temperatures. For NPs of about 10–14 nm, and assuming a pre-exponential time factor $\tau_0 \approx 10^{-9} s$ this experimental situation corresponds to effective anisotropy densities of the order of $3.5 \times 10^4 J/m^3 \leqslant K_{eff} \leqslant 9.5 \times 10^4 J/m^3$. These values are larger than magnetite or maghemite magnetocrystalline energies (1.1×10^4 to 1.25×10^4 J/m^3 for 200 K < T < 300 K for magnetite) [37], but typical of magnetite NPs of these sizes [39], due to anisotropy enhancement by surface effects.

5. Conclusions

Here we report for the first time the synthesis of quasi-spherical monocrystal iron oxide nanoparticles coated with an organic shell from a Yerba Mate aqueous extract. The organic shell thickness was susccessfully modified between 0 and 2 nm by varying the amount of Yerba Mate extract used, while the nanoparticles iron oxide core had their mean physical size at about 14–15 nm. The latter were determined with SAXS and TEM and were almost the same for all specimens. Magnetic sizes retrieved from M vs. H curves showed also little variation and were of 9–10 nm, while crystallite sizes determined by XRD decreased with increasing shell thickness, from about 15 to 11 nm. The characterization of the specimens with several techniques allowed to describe the structure of each NP core as a crystal iron oxide nucleus surrounded by a disordered iron oxide layer. The disordered oxide layer was not observed in the non-coated NPs but it was seen to increase monotonously with YM coating, achieving 1.7 nm for specimen YMD. The magnetic size however, did not coincide with the crystallite oxide one. The fact that the magnetic size is smaller than the physical one (the one observed by TEM and SAXS) and than the crystallite size (XRD), is assigned to the effect of dipolar interactions; the magnetic size of NP core in the YMD colloid specimen, in which the effect of dipolar interactions should be greatly reduced, is of 12.5 nm, larger by more than 3 nm than that of the powder specimen and closer to the physical size. The effect of interactions was also observed in the specimens' coercivities. As YM shell thickness increased from 0 to 1.7 nm, coercivity decreased from 830 to 110 A/m, while initial susceptibility showed

an increasing trend, varying from 6.3 to 7.1. It must be noticed that the observed coercive fields are small in comparison to the anisotropy field, which is of the order of 3.3×10^4 A/m in magnetite, and most probably are originated in the dipolar interaction among particles [32]. Comparison of room-temperature initial susceptibilities in YMD powder and colloid, of 7.1 and 17.7 respectively, highlights the influence of interactions in the former, where NPs are nearly in contact with each other, and can be understood by the existence of strong demagnetizing effects in the powder. Analysis of the interactions effect on the basis of the effective demagnetizing tensor model [19,20] leads to mean particle size to interparticle mean separation ratios of about 1.4–1.6, consistently with what would be expected for the specimens powder state configurations.

Acknowledgements

D.F.M. thanks Consejo Nacional de Investigaciones Científicas y Técnicas (CONICET, Argentina) for a graduate studentship. M.C.G. and F.H.S. are research members of CONICET. This work was funded by CONICET (PIP 11220110100720CO), ANPCyT (PICT-2012-2359), and UNLP-X11/680 grants of Argentina.

Appendix A. Supplementary data

Supplementary data associated with this article can be found, in the online version, at https://doi.org/10.1016/j.jmmm.2018.04.048.

References

[1] A.G. Roca, M.D.P. Morales, K. O'Grady, C.J. Serna, Structural and magnetic properties of uniform magnetite nanoparticles prepared by high temperature decomposition of organic precursors, Nanotechnology 17 (2006) 2783–2788, https://doi.org/10.1088/0957-4484/17/11/010.

[2] D.F. Mercado, G. Magnacca, M. Malandrino, A. Rubert, E. Montoneri, L. Celi, A. Bianco Prevot, M.C. Gonzalez, Paramagnetic iron-doped hydroxyapatite nanoparticles with improved metal sorption properties. A bioorganic substrates- mediated synthesis, ACS Appl. Mater. Interfaces 6 (2014) 3937–3946, https://doi.org/10.1021/am405217j.

[3] G. Magnacca, A. Allera, E. Montoneri, L. Celi, D.E. Benito, L.G. Gagliardi, M.C. Gonzalez, D.O. Mártire, L. Carlos, Novel magnetite nanoparticles coated with waste sourced bio- based substances as sustainable and renewable adsorbing materials, ACS Sustain. Chem. Eng. 2 (2014) 1518–1524, https://doi.org/10.1021/sc500213j.

[4] D.F. Mercado, A. Rubert, G. Magnacca, M. Malandrino, S. Sapino, P. Caregnato, A. Bianco Prevot, M.C. Gonzalez, Versatile Fe-containing hydroxyapatite nanomaterials as efficient substrates for lead ions adsorption, J. Nanosci. Nanotechnol 12 (2017) 9081–9090, https://doi.org/10.1166/jnn.2017.13870.

[5] P.M. Zélis, G. Pasquevich, S.J. Stewart, M.B.F. Van Raap, J. Aphesteguy, I.J. Bruvera, C. Laborde, B. Pianciola, S. Jacobo, F.H. Sánchez, Structural and magnetic study of zinc-doped magnetite nanoparticles and ferrofluids for hyperthermia applications, J. Phys. D Appl. Phys. 46 (2013) 125006, https://doi.org/10.1088/0022-3727/46/12/125006.

[6] M. Yamaura, R.L. Camilo, L.C. Sampaio, M.A. Macêdo, M. Nakamura, H.E. Toma, Preparation and characterization of (3-aminopropyl)triethoxysilane-coated magnetite nanoparticles, J. Magn. Magn. Mater. 279 (2004) 210–217, https://doi.org/10.1016/j.jmmm.2004.01.094.

[7] D.F. Coral, P. Mendoza Zélis, M. Marciello, M.D.P. Morales, A. Craievich, F.H. Sánchez, M.B. Fernández Van Raap, Effect of nanoclustering and dipolar interactions in heat generation for magnetic hyperthermia, Langmuir 32 (2016) 1201–1213, https://doi.org/10.1021/acs.langmuir.5b03559.

[8] R.A. Sperling, T. Liedl, S. Duhr, S. Kudera, M. Zanella, C.-A.J. Lin, W.H. Chang, D. Braun, W.J. Parak, Size determination of (Bio)conjugated water-soluble colloidal nanoparticles: a comparison of different techniques, J. Phys. Chem. C 111 (2007) 11552–11559, https://doi.org/10.1021/jp070999d.

[9] M.E. De Sousa, M.B. Fernández van Raap, P.C. Rivas, P. Mendoza Zélis, P. Girardin, G.A. Pasquevich, J.L. Alessandrini, D. Muraca, F.H. Sánchez, Stability and relaxation mechanisms of citric acid coated magnetite nanoparticles for magnetic hyperthermia, J. Phys. Chem. C 117 (2013) 5436–5445, https://doi.org/10.1021/jp311556b.

[10] T.M. Petrova, L. Fachikov, J. Hristov, The Mag As adsorbe for some hazardous species from aqueous solutio a review, Int. Rev. Chem. Eng. Int. Rev. Chem. Eng. 3 (2011) 134–152.

[11] P. Kingshott, J. Wei, D. Bagge-Ravn, N. Gadegaard, L. Gram, Covalent attachment of poly(ethylene glycol) to surfaces, critical for reducing bacterial adhesion, Langmuir 19 (2003) 6912–6921, https://doi.org/10.1021/la034032m.

[12] R.A. Revia, M. Zhang, Magnetite nanoparticles for cancer diagnosis, treatment, and treatment monitoring: recent advances, Mater. Today 19 (2016) 157–168, https://doi.org/10.1016/j.mattod.2015.08.022.

[13] N. Andhariya, B. Chudasama, R.V. Mehta, R.V. Upadhyay, Nanoengineering of methylene blue loaded silica encapsulated magnetite nanospheres and nanocapsules for photodynamic therapy, J. Nanoparticle Res. 13 (2011) 3619–3631, https://doi.org/10.1007/s11051-011-0279-1.

[14] S. Iravani, Green synthesis of metal nanoparticles using plants, Green Chem. 13 (2011) 2638–2650, https://doi.org/10.1039/c1gc15386b.

[15] D.F. Mercado, P. Caregnato, L. Villata, M.C. Gonzalez, Ilex paraguariensis extract – coated magnetite nanoparticles: a sustainable nano-adsorbents and antioxidant, J. Inorg. Organometal. Polym. Mater. 28 (2018) 519–527, https://doi.org/10.1007/s10904-017-0757-8.

[16] S. Morup, E. Tronc, Superparamagnetic relaxation of weakly interacting particles, Phys. Rev. Lett. 72 (1994) 3278–3281, https://doi.org/10.1103/PhysRevLett. 72.3278.

[17] G.T. Landi, The random dipolar-field approximation for systems of interacting magnetic particles, J. Appl. Phys. 113 (2013) 163908, https://doi.org/10.1063/1.4802583.

[18] P. Allia, M. Coisson, P. Tiberto, F. Vinai, M. Knobel, M.A. Novak, W.C. Nunes, Granular Cu-Co alloys as interacting superparamagnets, Phys. Rev. B – Condens. Matter Mater. Phys. 64 (2001) 1444201–14442012, https://doi.org/10.1103/PhysRevB.64.144420.

[19] F.H. Sánchez, P. Mendoza Zélis, M.L. Arciniegas, G.A. Pasquevich, M.B. Fernández Van Raap, Dipolar interaction and demagnetizing effects in magnetic nanoparticle dispersions: introducing the mean-field interacting superparamagnet model, Phys. Rev. B. 95 (2017) 1–18, https://doi.org/10.1103/PhysRevB.95.134421.

[20] P. Mendoza Zélis, V. Vega, V.M. Prida, L.C. Costa-Arzuza, F. Béron, K.R. Pirota, R. López-Ruiz, F.H. Sánchez, Effective demagnetizing tensors in arrays of magnetic nanopillars, Phys. Rev. B 96 (2017) 174427, https://doi.org/10.1103/PhysRevB.96.174427.

[21] G. Mériguet, E. Dubois, M. Jardat, A. Bourdon, G. Demouchy, V. Dupuis, B. Farago, R. Perzynski, P. Turq, Understanding the structure and the dynamics of magnetic fluids: coupling of experiment and simulation, J. Phys. Condens. Matter. 18 (2006) S2685–S2696, https://doi.org/10.1088/0953-8984/18/38/S11.

[22] G. Beaucage, Small-angle scattering from polymeric mass fractals of arbitrary mass-fractal dimension, J. Appl. Crystallogr. 29 (1996) 134–146, https://doi.org/10.1107/S0021889895011605.

[23] G. Beaucage, Approximations leading to a unified exponential/power-law approach to small-angle scattering, J. Appl. Crystallogr. 28 (1995) 717–728, https://doi.org/10.1107/S0021889895005292.

[24] W. Kim, C.-Y. Suh, S.-W. Cho, K.-M. Roh, H. Kwon, K. Song, I.-J. Shon, A new method for the identification and quantification of magnetite–maghemite mixture using conventional X-ray diffraction technique, Talanta 94 (2012) 348–352, https://doi.org/10.1016/j.talanta.2012.03.001.

[25] P. Allia, M. Coisson, P. Tiberto, F. Vinai, Hysteretic magnetisation curves in the granular Cu 100-x Co x system, Nanostruct. Mater. 11 (1999) 757–767. http://www.sciencedirect.com/science/article/pii/S0965977399003645.

[26] T. Jonsson, J. Mattsson, P. Nordblad, P. Svedlindh, Energy barrier distribution of a noninteracting nano-sized magnetic particle system, J. Magn. Magn. Mater. 53 (1986) 404–407.

[27] G.T. Landi, Role of dipolar interaction in magnetic hyperthermia, Phys. Rev. B – Condens. Matter Mater. Phys. 89 (2014) 0144031–0144036, https://doi.org/10.1103/PhysRevB.89.014403.

[28] R.K. Das, S. Rawal, D. Norton, A.F. Hebard, A collective dynamics description of dipolar interactions and the coercive field of magnetic nanoparticles, J. Appl. Phys. 108 (2010) 1239201–1239205, https://doi.org/10.1063/1.3524277.

[29] C. Djurberg, P. Svedlindh, P. Nordblad, M. Hansen, F. Bødker, S. Mørup, Dynamics of an interacting particle system: evidence of critical slowing down, Phys. Rev. Lett. 79 (1997) 5154–5157, https://doi.org/10.1103/PhysRevLett.79.5154.

[30] J.L. Dormann, L. Bessais, D. Fiorani, A dynamic study of small interacting particles: superparamagnetic model and spin-glass laws, J. Phys. C Solid State Phys. 21 (1988) 2015–2034, https://doi.org/10.1088/0022-3719/21/10/019.

[31] P. Allia, M. Coisson, M. Knobel, P. Tiberto, F. Vinai, Magnetic hysteresis based on dipolar interactions in granular magnetic systems, Phys. Rev. B. 60 (1999) 12207–12218, https://doi.org/10.1103/PhysRevB.60.12207.

[32] M. Klokkenburg, B.H. Erné, A. Wiedenmann, A.V. Petukhov, A.P. Philipse, Dipolar structures in magnetite ferrofluids studied with small-angle neutron scattering with and without applied magnetic field, Phys. Rev. E – Stat. Nonlinear Soft Matter Phys. 75 (2007) 0514081–0514089, https://doi.org/10.1103/PhysRevE.75.051408.

[33] S. Nakamae, C. Crauste-Thibierge, D. L'Hôte, E. Vincent, E. Dubois, V. Dupuis, R. Perzynski, Dynamic correlation length growth in superspin glass: bridging experiments and simulations, Appl. Phys. Lett. 101 (2012) 2424091–2424097, https://doi.org/10.1063/1.4769840.

[34] R. Kaiser, G. Miskolczy, Magnetic properties of stable dispersions of subdomain magnetite particles, J. Appl. Phys. 41 (1970) 1064–1072, https://doi.org/10.1063/1.1658812.

[35] A. Aharoni, Demagnetizing factors for rectangular ferromagnetic prisms, J. Appl. Phys. 83 (1998) 3432–3434, https://doi.org/10.1063/1.367113.

[36] B.D. Cullity, C.D. Graham, Introduction to Magnetic Materials, IEEE/Wiley, Hoboken, 2009.

[37] R. Reznícek, V. Chlan, H. Stepánkova, P. Povák, M. Marysko, Magnetocrystalline anisotropy of magnetite, J. Magn. Magn. Mater. 24 (2012) 0555011–0555017, https://doi.org/10.1016/0304-8853(83)90698-4.

[38] R.P. Tan, J. Carrey, M. Respaud, Magnetic hyperthermia properties of nanoparticles inside lysosomes using kinetic Monte Carlo simulations: influence of key parameters and dipolar interactions, and evidence for strong spatial variation of heating power, Phys. Rev. B – Condens. Matter Mater. Phys. 90 (2014) 2144211–21442112, https://doi.org/10.1103/PhysRevB.90.214421.

[39] Y. Sunghyun, Determination of the temperature dependence of the magnetic anisotropy constant in magnetite nanoparticles, J. Korean Phys. Soc. 59 (2011) 3069–3073, https://doi.org/10.3938/jkps.59.3069.